A 2π spectrometer for electron–electron coincidence studies on surfaces

M. Hattass,[a] T. Jalowy, A. Czasch, Th. Weber, T. Jahnke, S. Schössler, L. Ph. Schmidt, O. Jagutzki, R. Dörner, and H. Schmidt-Böcking
Institut für Kernphysik, J. W. Goethe Universität Frankfurt, August-Euler-Str.6, 60486 Frankfurt, Germany

(Received 18 December 2003; accepted 5 April 2004; published online 21 June 2004)

We present a new time-of-flight spectrometer for energy and angle-resolved measurements of electrons emitted in coincidence from a surface. By using a projection method, we can cover nearly 2π of the solid angle above the sample resulting in a very high coincidence efficiency. The use of this new spectrometer for the double photoemission process from surfaces will be demonstrated. © *2004 American Institute of Physics.* [DOI: 10.1063/1.1765764]

I. INTRODUCTION

The demand in atomic and molecular physics for highly differential cross sections in numerous reaction systems like ion-atom collisions[1,2] and photodouble ionization of atoms and molecules[3,4] led to the development of sophisticated imaging and coincidence techniques,[5–7] see Refs. 8 and 9 for a recent review. All of these methods are based on time-of-flight (TOF) systems combined with position sensitive detectors. The main advantage of this technique lies in the wide angular acceptance compared to ''classical'' angle and energy scanning spectrometers. As the coincidence rate scales with the solid angle Ω^N, where Ω is the solid angle and N the number of particles to be coincidentally detected, coincidence experiments become a very tedious task for small solid angles.

For the spectroscopy of electrons produced in reactions on solids and surfaces, there are only few experiments exploiting coincidence methods like $(e,2e)$ reactions in forward[10,11] and backscattering geometries.[12,13] Using synchrotron light as an excitation source, Auger-photoelectron-coincidence spectroscopy (Refs. 14 and 15) is a growing field of interest. Also, experiments on $(\gamma,2e)$ reactions from valence-band states[16] have been reported. Despite their success, all of these experiments suffer from very low coincidence rates. In this article, we present a novel spectrometer type for coincidence electron spectroscopy from surfaces which applies the established imaging techniques from gas targets to electron emission from surfaces.

II. SPECTROMETER

Figure 1 shows a sketch of the spectrometer. The target is mounted on a four-axis manipulator and can be moved through an opening into the spectrometer. The beam enters through a slit in the side electrodes and hits the target under an angle of 45°. The electrons are extracted from the target by a weak electric field in the order of a few V/cm and accelerated over a distance of 26 cm toward the position sensitive multichannel plate detector (80 mm diameter). The electron flight times are typically <100 ns. To collect electrons up to ~ 50 eV emitted into 2π of the solid angle a parallel magnetic field of ~ 10 Gauß is applied by a pair of Helmholtz coils which is located outside the vacuum chamber.[5]

The electron trajectory in the spectrometer is given by the parallel electric and magnetic fields and the initial velocity. The equation of motion in this setup is (with E_z, B_z, the components of the electric and magnetic field on the spectrometer axis and q_e, m_e the electron charge and mass)

$$\begin{aligned} m_e\ddot{x} &= q_e\dot{y}B_z, \\ m_e\ddot{y} &= -q_e\dot{x}B_z, \\ m_e\ddot{z} &= q_eE_z. \end{aligned} \tag{1}$$

Equation (1) integrated and solved for the initial velocities yields (x,y: Electron impact position on detector, t: electron's TOF)

$$\begin{aligned} v_x &= \frac{-xa-by}{a^2+b^2}, \\ v_y &= \frac{xb-ay}{a^2+b^2}, \\ v_z &= \frac{s}{t} - \frac{q_eE_z}{2m_e}t, \end{aligned} \tag{2}$$

where

$$a = \frac{1-\cos\omega t}{\omega}, \quad b = \frac{\sin\omega t}{\omega}, \tag{3}$$

s is the length of the acceleration region and ω is the cyclotron frequency of the electron in the applied magnetic field. An example of electron trajectories for electron energies of 40 eV and various emission angles in respect to the surface normal is shown in Fig 2.

The resolution of the spectrometer for momenta parallel to the surface is determined by the beam spot size on the sample and the spatial resolution of the detector (Δr), the distance of the impact position from the spectrometer axis r, as well as the electron TOF t in respect to the cyclotron frequency ω in the magnetic field. The momentum resolution $\Delta k_{\parallel}$ is given by

[a]Electronic mail: hattass@hsb.uni-frankfurt.de

$$\Delta k_{\parallel}=\frac{m_e\omega}{2}\sqrt{\left[|\Delta r|\sqrt{1+\left(\frac{\sin\omega t}{1-\cos\omega t}\right)^2}\right]^2+\left(r|\Delta t|\sqrt{\left[\frac{\omega\cos\omega t}{1-\cos\omega t}-\frac{\omega\sin^2\omega t}{(1-\cos\omega t)^2}\right]^2}\right)^2}. \tag{4}$$

In the present case $|\Delta r|=0.3$ mm (the spatial resolution of the position sensitive detector) and $\omega=1.9\times10^8\ \mathrm{s}^{-1}$ (cyclotron frequency of the applied magnetic field). By adjusting the TOF by tuning the electric field, one can achieve a momentum resolution of about $\Delta k_{\parallel}=0.013$ a.u. (a.u. = atomic units $m_e=\hbar=e=1$).

Along the spectrometer axis, the resolution is given by the overall TOF of the electron t, the magnitude of the electric extraction field E_z, and the timing resolution of the detector and the time-to-digital converter (TDC) ($\Delta t=0.5$ ns):

$$\Delta k_{\perp}=\sqrt{\left(\frac{s}{t^2}+\frac{q_eE_z}{2m_e}\right)^2(\Delta t)^2}. \tag{5}$$

Typical values are $\Delta k_{\perp}=0.01$ a.u. at $k_{\perp}=0.5$ a.u., and $\Delta k_{\perp}=0.03$ a.u. at $k_{\perp}=2.0$ a.u.

Figure 3 gives an overview on the dependency of the angular and energy resolution on electron energy and polar emission angle. The diagrams are calculated for an electric field of 7.8 V/cm and a magnetic field of 10.8 Gauß.

Due to the 2π collection angle the coincidence efficiency of this spectrometer is significantly higher than in other conventional setups. Assuming two electrostatic analyzers with a realistic opening angle of 5° one arrives—just considering the accessible solid angle—at a coincidence efficiency in the order of 10^{-6}, whereas it is nearly 1 in our case. Nevertheless, this number is reduced by the detection efficiency of the detector. For a two-electron event, this amounts to roughly 0.1 which still leaves five orders of magnitude to a conventional system.

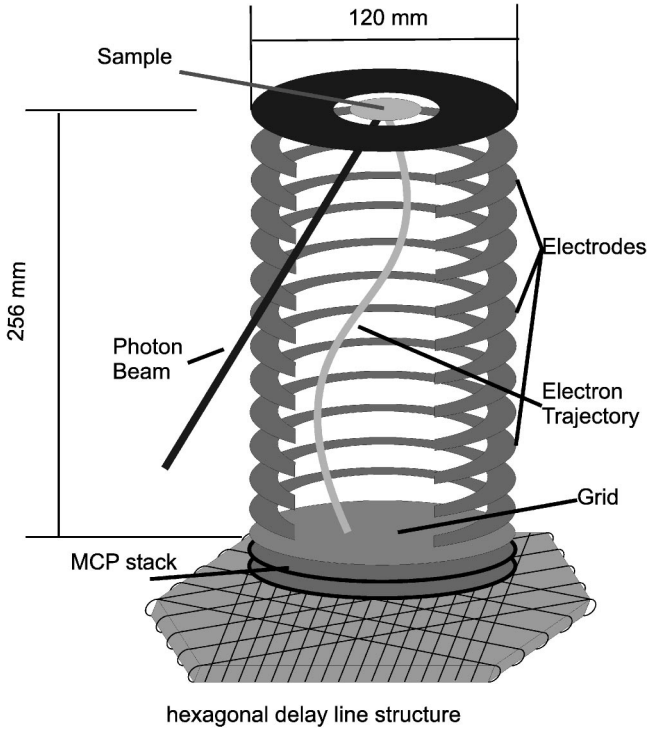

FIG. 1. Sketch of the TOF spectrometer. Parallel homogeneous E and B fields are used to extract electrons from the target and project them onto a position and time sensitive multichannel plate detector. The photon beam enters from the left into the spectrometer through a slit in the side electrodes.

III. DETECTOR

Since the maximal difference of TOFs between the fastest (~50 eV) and the slowest (0 eV) electrons in this spectrometer is in the order of only ≤50 ns, the ability of the detector to accept multiple hits is crucial for a successful coincidence measurement. To achieve a high multihit detection and accurate position determination, we use a multichannel plate (MCP) detector with a delay-line readout. The basic principle of the position determination with the delay-line detector is shown in Fig. 4(a). The charge cloud from the MCP is collected on a delay-line anode structure where it forms two pulses propagating toward the respective ends of the cable. The position information is obtained by subtracting the individual run times $t_{1,2}$ which are measured in respect to the trigger pulse of the MCP t_{MCP} ($\Delta t_{1,2}=t_{\mathrm{MCP}}-t_{1,2}$), e.g.,

$$x=(\Delta t_1-\Delta t_2)c, \tag{6}$$

where c is the propagation speed on the delay line. This is the situation for detecting single electrons. If more than one electron has to be detected within a very short time [Fig. 4(b)], the signals from different electrons may mix at the end of the delay line, i.e., the second detected anode signal at one end belongs to the first electron and vice versa at the other end. Which signals on the different delay-line ends correspond to each other can be easily found by determining the time sums of the signal run times at both ends. Since the propagation time over the whole delay line is a constant, the sum of matching signals is always fixed:

$$t_{\mathrm{sum}}=\Delta t_1+\Delta t_2=\text{constant}. \tag{7}$$

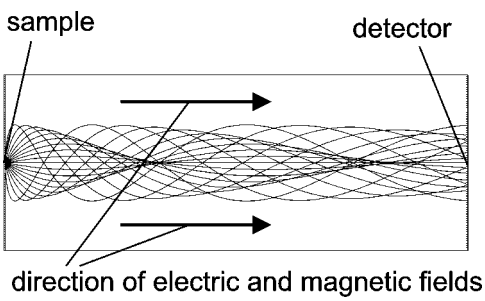

FIG. 2. Example for electron trajectories at 40 eV kinetic energy and various emission angles calculated with SIMION 7.0. The electric field is 7.8 V/cm, the magnetic field 10.8 Gauß.

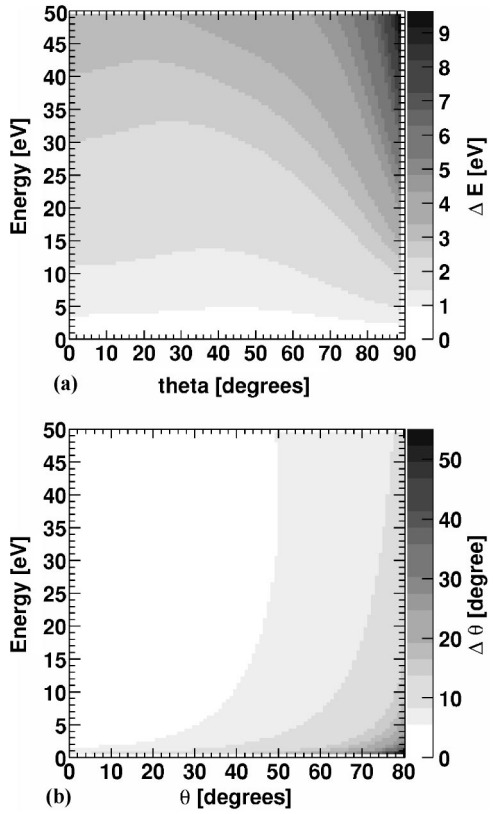

FIG. 3. (a) Energy resolution ΔE as a function of energy and polar angle of the emitted electron. The energy resolution in eV is given as gray scale coding on the z axis. Values have been calculated for an extraction field of 7.8 V/cm and a magnetic field of 10.8 Gauß. (b) Angular resolution (polar angle) $\Delta\Theta$ as a function of energy and polar angle of the emitted electron. The resolution in degrees is given as gray scale coding on the z axis, same field settings as in (a).

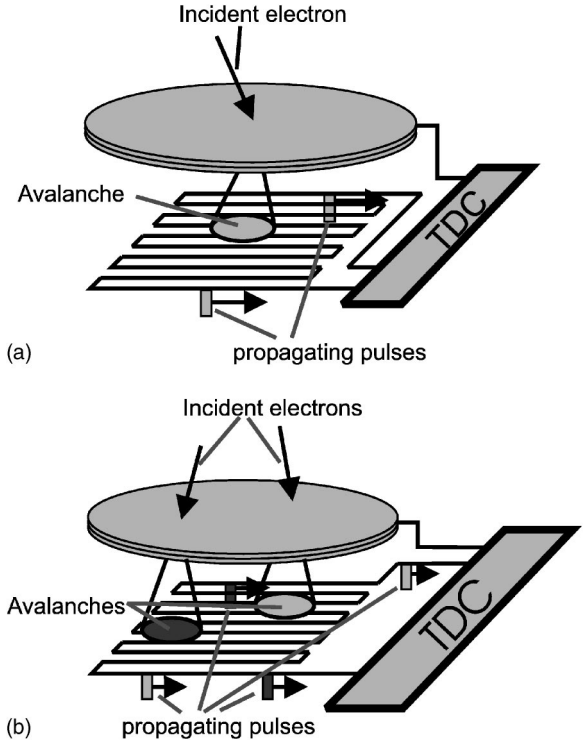

FIG. 4. (a) Single electron detection with the delay-line detector: The electron cloud from the MCP is collected on the anode wires and propagates toward the respective ends. The position determination is achieved by subtracting the run times. (b) Detection of two electrons which arrive at the detector at nearly the same time. The timing signal order on the anode mixes but can be corrected in the off-line analysis.

This relation can be used to identify signals originating from different electrons. By checking the sums $t_{1\,\mathrm{hit}\,1}+t_{2\,\mathrm{hit}\,1}$ against $t_{1\,\mathrm{hit}\,1}+t_{2\,\mathrm{hit}\,2}$ in the analysis, one can by a resorting algorithm account for the mixing.

In principle, two independent delay-line layers would be enough to determine the x and y positions of the electron impact. However, we are using a three-layer anode.[17,18] Here, the additional layer creates a redundancy which reduces the dead time for multiparticle detection. This is necessary if the separation of the pulses is in the order of the signal width ($\sim$8 ns). The redundancy can be used to reconstruct signals, e.g., the MCP signal, via the anode signals. If two electrons hit the detector nearly at the same time, only 1 MCP signal will be detected. However, if the electrons are separated sufficiently in position, the anode signals are still separated. Now, the known time sums (which are a constant for the detector arrangement) can be used to reconstruct the missing MCP signal by using the relation

$$t_{\mathrm{MCP}}=\tfrac{1}{2}(t_1+t_2-t_{\mathrm{sum}}). \tag{8}$$

The same holds for signals on the anode wires if the separation in arrival time is sufficient, but the separation of the pulses on the anode is not large enough on all anode layers. Except for a small area around or a short time after the first hit, the detection of two electrons is possible. In this experiment, the dead region is limited to a spot of about 5 mm diameter around the first hit, and a time of about 8 ns after the first hit which is sufficient for our purpose. This experimental setup has been designed to detect 2 electrons fully momentum resolved. Depending on the spread in TOF as well as the time resolution the (momentum-resolved and coincident) detection of up to four electrons should be possible.

All timing signals (anode signals and MCP signal), with respect to the start signal by the synchrotron, are fed into an eight-channel multihit TDC which is run in common-stop mode.

IV. EXPERIMENT

First experiments with this setup have been performed at beamline BW3 at HASY-LAB/DESY in Hamburg with photons in the energy range from 40 to 100 eV. The target was a single-crystal Cu(111) surface which was cleaned by Ar^+ sputtering and annealing cycles. To prevent background produced by the detection of uncorrelated electron pairs that have been created by two photons within one bunch of the synchrotron pulse (repetition frequency 5 MHz) the single-electron detection rate was always kept below 2 kHz. Because of this very low photon rate, space-charge effects also do not play a role in this experiment. Figure 5 shows an angle-integrated electron TOF spectrum in the case of 40 eV photons hitting the surface. The sharp cutoff for low flight times ($\sim$44 ns) corresponds to electrons originating from near the Fermi level. The cutoff for long TOFs ($\sim$65 ns) is

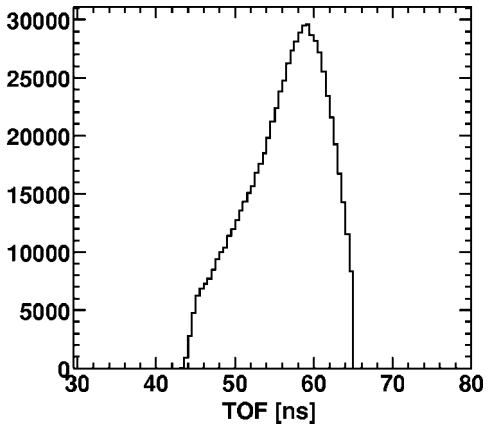

FIG. 5. Angle-integrated TOF spectrum for $\hbar\omega = 40$ eV. The low-energy cutoff lies at 65 ns while the fastest electrons originating from the Fermi level have a minimum flight time of 44 ns.

due to the electric field which defines a maximum flight time for 0 eV electrons. Combined with the position information (Fig. 6), the spectra show a periodic pattern which reflects the cyclotron motion of the electrons along the spectrometer axis. For flight times being multiples of the cyclotron period ($T = 33$ ns), all trajectories are being refocused to a single point in the $x-y$ plane. This fact can also be used as a very precise calibration of the magnetic field and the time zero by interpolating over several of these knots. Furthermore, it can be used to adjust the relative alignment of the electric and magnetic field. If the electric and magnetic fields are not parallel, the focus points will move as a function of flight time in the $x-y$ plane. The explicit shielding of the earth's magnetic field is also not necessary. Only the effective field, which is the sum of the applied field $\mathbf{B}_{\text{applied}}$ and the earth's field $\mathbf{B}_{\text{earth}}$ matters for the experiment. Since $\mathbf{B}_{\text{applied}}$ is typically much larger than $\mathbf{B}_{\text{earth}}$ (10 Gauß compared to 0.5 Gauß), the resulting field $\mathbf{B}_{\text{eff}} = \mathbf{B}_{\text{applied}} + \mathbf{B}_{\text{earth}}$ can be easily controlled to be exactly parallel to $\mathbf{E}$ by the method described above. However, inhomogenities in the magnetic and electric field have to be avoided. The electric field is determined by the applied voltages on the resistor chain which connects the electrodes. This value can be fine tuned by

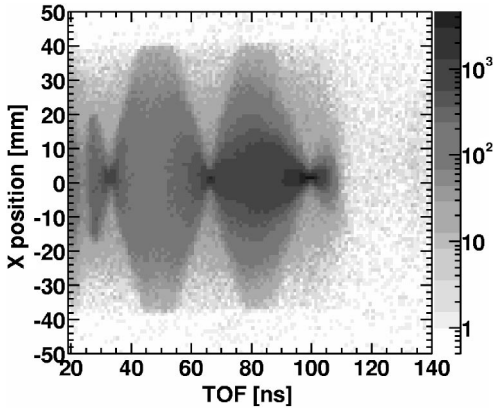

FIG. 6. X position on the detector vs TOF for a low extraction field (0.2 V/cm). The magnetic field induces a cyclotron motion on the electron trajectory which is refocused to a single point with the periodicity of the cyclotron frequency.

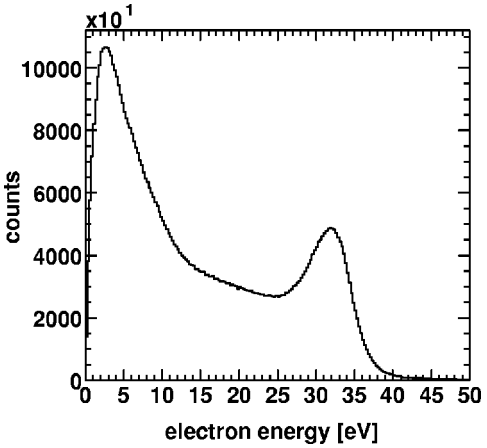

FIG. 7. Angle-integrated electron energy distribution for $\hbar\omega = 40$ eV on Cu(111). The peak at ~32 eV stems from the Cu $3d$ valence band while the secondary electron maximum lies at 2–3 eV.

looking at the electrons (from single photoemission) with normal emission direction and comparing their energy spectrum with literature values. Furthermore, when working with higher photon energies, one can use electrons from excited core levels whose kinetic energies are just given by their binding energy and the photon energy to calibrate the electric field.

All measured position and time information for each electron are stored event by event in a list mode file using the COBOLD data acquisition software.[18] Angles and energies are being calculated later in the off-line data analysis.

V. RESULTS FOR SINGLE PHOTOEMISSION

Figure 7 shows an energy spectrum for 40 eV photons which can be obtained by reconstructing the initial momenta from the time and position information knowing the electric and magnetic fields. Visible in this angle-integrated spectra is the energy distribution for single-photoelectron emission. It shows the emission from valence-band states at around 32 eV while the maximum of secondary electron emission is at about 2–3 eV.

Since the complete momentum distribution is measured, we can also create angle-resolved spectra of the valence-band photoemission. Figure 8 shows the momenta parallel to the surface for emission from binding energies from 0 to 10 eV. The photon incidence angle is 45° and the polarization lies in the Y plane. The periodic pattern visible in this momentum plot reflects the symmetry of the Cu(111) surface while the increasing intensity toward the positive y axis is due to the off-normal incidence of the photon beam.

VI. RESULTS FOR DOUBLE PHOTOEMISSION

Applying coincidence conditions on the angle-integrated energy spectrum (Fig. 7), i.e., requiring a second electron to be emitted for one incident photon, the spectra yield a very different shape (Fig. 9). The structure from the valence-band photoemission vanishes completely, leaving a steeply rising structure toward lower energies. This can be explained by the fact that the photon energy now has to be shared between the two emitted electrons. The energy sharing can be seen in

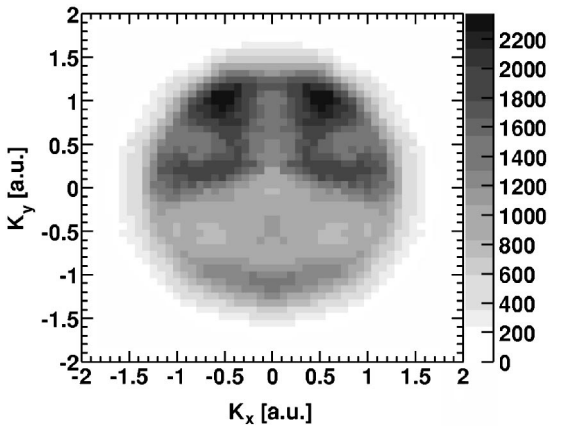

FIG. 8. Momentum plot of photoemission from valence-band states in Cu(111) (integrated over binding energies from 0–10 eV). $K_{x,y}$ are the momentum components parallel to the sample surface. The polarization of the photons of $\hbar\omega = 40$ eV lies in the $Y-Z$ plane.

more detail in Fig. 10. Plotted in Fig. 10 is the energy of one detected electron against the energy of the second coincident electron. The triangular shape is due to energy conservation: Because the photon energy has to be shared between the two electrons, the maximum available sum energy (constant sum energies correspond to diagonal lines from the upper left to the lower right corner in Fig 10) is fixed. As the electron pair is created inside the solid, both electrons furthermore have to overcome the surface barrier of ~ 5 eV. The position of the high-energy cutoff can thus be given as $E_{\mathrm{sum}} \leqslant E_{\mathrm{phot}} - 2W_{\phi}$ (with the work function W_{ϕ}). Electrons emitted with sum energies close to this threshold originate from states close to the Fermi level, i.e., 0 eV binding energy. Electron pairs with lower sum energies either stem from valence-band states with larger binding energies or must have suffered energy loss by inelastic scattering inside the solid. Assuming a self-convolution of the single-electron band structure to obtain the allowed levels for double-photoelectron emission gives a lower-energy limit of $E_{\mathrm{sum}} = 10$ eV for the electron pairs which left the solid without any energy loss. Below this energy, the electrons can be seen as part of a typical secondary electron cascade. The ratio of two-electron emission (including inelastic scattering events) to the emission of a single

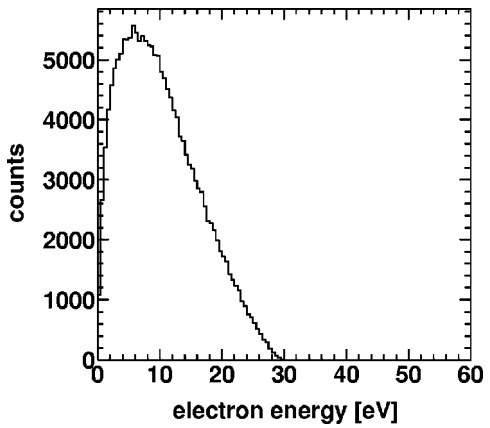

FIG. 9. Energy spectrum of a coincident electron in the same configuration as in Fig 7. The spectrum is integrated over all properties of the corresponding partner electron.

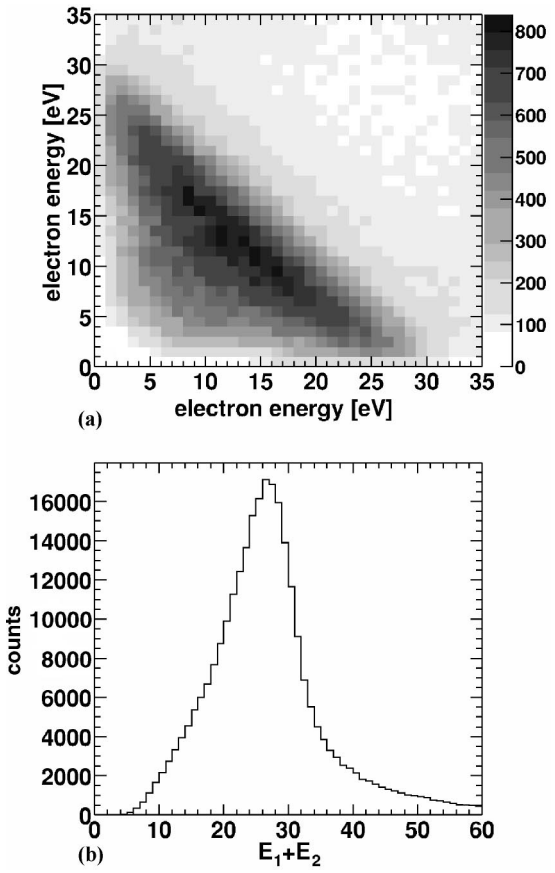

FIG. 10. (a) Coincident energy–energy spectrum for $\hbar\omega = 40$ eV. Cutoff energy is at about ~ 30 eV. (b) Corresponding sum energy ($E_1 + E_2$) spectrum.

electron at 40 eV photon energy can be estimated from our data. Including corrections for the detection efficiency one arrives at a value of about 1%.

ACKNOWLEDGMENTS

The authors would like to thank C. Winkler and J. Kirschner from the Max-Planck Institut für Mikrostrukturphysik in Halle for providing the Cu sample and equipment during the experiment as well as valuable discussions. This work was supported, in part, by the Bundesministerium für Bildung und Forschung (BMBF).

[1] R. Moshammer, J. Ullrich, H. Kollmus, W. Schmitt, M. Unverzagt, H. Schmidt-Böcking, C. J. Wood, and R. E. Olson, Phys. Rev. A **56**, 1351 (1997).
[2] M. Schulz, R. Moshammer, W. Schmitt, H. Kollmus, R. Mann, S. Hagmann, R. E. Olson, and J. Ullrich, Phys. Rev. A **61**, 022703 (2000).
[3] R. Dörner, J. M. Feagin, C. L. Cocke, H. Bräuning, O. Jagutzki, M. Jung, E. P. Kanter, H. Khemliche, S. Kravis, V. Mergel, M. H. Prior, H. Schmidt-Böcking, L. Spielberger, J. Ullrich, M. Unversagt, and T. Vogt, Phys. Rev. Lett. **77**, 1024 (1996).
[4] R. Dörner, H. Bräuning, O. Jagutzki, V. Mergel, M. Achler, R. Moshammer, J. M. Feagin, T. Osipov, A. Bräuning-Demian, L. Spielberger, J. H. McGuire, M. H. Prior, N. Berrah, J. D. Bozek, C. L. Cocke, and H. Schmidt-Böcking, Phys. Rev. Lett. **81**, 5776 (1998).
[5] R. Moshammer, J. Ullrich, M. Unverzagt, W. Schmitt, and H. Schmidt-Böcking, Nucl. Instrum. Methods Phys. Res. B **108**, 425 (1996).
[6] J. Ullrich, R. Moshammer, R. Dörner, O. Jagutzki, V. Mergel, H. Schmidt-Böcking, and L. Spielberger, J. Phys. B **30**, 2917 (1997).
[7] M. Schulz, R. Moshammer, D. Fischer, H. Kollmus, D. H. Madison, S.

Jones, and J. Ullrich, Nature (London) **422**, 48 (2003).
[8] R. Dörner, V. Mergel, O. Jagutzki, L. Spielberger, J. Ullrich, R. Moshammer, and H. Schmidt-Böcking, Phys. Rep. **330**, 95 (2000).
[9] J. Ullrich, R. Moshammer, A. Dorn, R. Dörner, L. P. H. Schmidt, and H. Schmidt-Böcking, Rep. Prog. Phys. **66**, 1463 (2003).
[10] M. Vos, Z. Fang, S. Canney, A. Kheifets, I. E. McCarthy, and E. Weigold, Phys. Rev. B **56**, 963 (1997).
[11] X. Guo, Z. Fang, A. S. Keifets, S. A. Canney, M. Vos, I. E. McCarthy, and E. Weigold, Phys. Rev. B **57**, 6333 (1998).
[12] J. Kirschner, O. A. Artamonov, and A. N. Terekhov, Phys. Rev. Lett. **69**, 1711 (1992).
[13] R. Feder, H. Gollisch, D. Meinert, T. Scheunemann, O. M. Artamonov, S. N. Samarin, and J. Kirschner, Phys. Rev. B **58**, 16418 (1998).
[14] H. W. Haak, G. A. Sawatzky, and T. D. Thomas, Phys. Rev. Lett. **41**, 1825 (1978).
[15] R. A. Bartynski, E. Jensen, S. L. Hubert, and C. C. Kao, Prog. Surf. Sci. **53**, 155 (1996).
[16] R. Herrmann, S. Samarin, H. Schwabe, and J. Kirschner, Phys. Rev. Lett. **81**, 2148 (1998).
[17] O. Jagutzki, A. Cerezo, A. Czasch, R. Dörner, M. Hattass, M. Huang, V. Mergel, U. Spillmann, K. Ullmann-Pfleger, T. Weber, H. Schmidt-Böcking, and G. D. W. Smith, IEEE Trans. Nucl. Sci. **49**, 2477 (2002).
[18] For details about the data acquisition software please check the COBOLD PC manual available at www.roentdek.com